

Internally coupled metamaterial beam for simultaneous vibration suppression and low frequency energy harvesting

Guobiao Hu,¹ Lihua Tang,^{1,a)} and Raj Das²

¹Department of Mechanical Engineering, University of Auckland, 20 Symonds Street, Auckland 1010, New Zealand

²School of Engineering, RMIT University, GPO Box 2476, Melbourne VIC 3001, Australia

(Received 3 November 2017; accepted 17 January 2018; published online 6 February 2018)

The paper proposes a modified metamaterial beam for simultaneous vibration suppression and energy harvesting. Local resonators in the modified metamaterial beam are alternately coupled, and each resonator is associated with a piezoelectric element for converting vibrations into electrical energy. First, the mathematical model of the modified metamaterial beam based piezoelectric energy harvester (PEH) is developed. The vibration suppression and energy harvesting performances of this system are analysed and compared with those of a conventional metamaterial beam PEH. The analytical results predict that not only the energy harvesting performance can be massively reinforced in the low frequency range, but also the vibration suppression performance can be slightly enhanced due to the appearance of an additional band gap. Subsequently, two finite element models, Models A and B, are developed. Model A is expected to be equivalent to the analytical model for validation and the local oscillators represented by lumped parameters in the analytical model are modelled by using cantilevers with tip masses. These tip masses are alternately coupled with ideal springs. The finite element analysis results in terms of both vibration suppression and energy harvesting show good agreement with the analytical results. Finally, to propose a more practical design of the internal coupling, Model B is established. Every two neighbouring tip masses are alternately coupled by using a beam connection. The finite element analysis results show that Model B is not completely equivalent to the proposed analytical model: no significant enhancement in terms of energy harvesting but a remarkably enhanced vibration suppression performance.

Published by AIP Publishing. <https://doi.org/10.1063/1.5011999>

I. INTRODUCTION

Elastic metamaterials (EMMs) with artificially engineered microstructures possess several unique properties including negative refraction,^{1,2} negative modulus,^{3,4} negative effective density,^{5,6} to name a few. Researchers have been attracted to explore the applications of EMMs for various kinds of applications,^{7–11} one of which is low frequency vibration suppression.^{12–15} The ability of EMMs for vibration suppression arises from their band gap phenomenon due to the out-of-phase motion of the introduced microstructures (local resonators) when vibrations occur near resonance.^{16,17}

Yao *et al.*⁵ performed an experimental study to reveal this mechanism. Huang *et al.*⁶ presented an analytical study of one dimensional elastic metamaterials based on spring-mass lumped parameter modelling. Liu *et al.*¹³ proposed a method based on the Euler-Bernoulli beam theory in conjunction with the transfer matrix method (TMM) for calculating the band structures of metamaterial beams. Based on the Timoshenko beam theory in conjunction with the transfer matrix method (TMM), Yu *et al.*¹⁸ proposed a similar method for calculating the band structures of metamaterial beams. Zhu *et al.*¹² applied the Timoshenko beam theory and calculated the band structure of a modified metamaterial beam with multiple embedded local resonators. Pai¹⁹ adopted another method

based on the combination of the beam theory and the Bloch's theorem to derive the dispersion relation of a metamaterial beam. Recently, Sugino *et al.*²⁰ proposed a novel method for estimating the band gaps of metamaterial beams based on modal analysis in conjunction with the assumption of infinite number of resonators.

In addition to the methodology development for band structure analysis, other researchers attempted to explore the ways to widen the band gap of acoustic metamaterials or make it tuneable for achieving modified metamaterials with enhanced vibration suppression performance.²¹ Huang and Sun.²² introduced a multiple resonators embedded metamaterial, whose each cell contains three masses connected in series by linear springs. This proposed modified metamaterial can provide multiple band gaps for vibration suppression. Chen *et al.*²³ proposed a band gap tunable metamaterial, whereby the tunability was realized through connecting the inner mass to the outer mass in each cell by a piezoelectric element that is shunted to a negative capacitance circuit. A recent work by Hu *et al.*²⁴ was also based on a similar idea and presented a piezoelectric tunable metamaterial. The analytical model developed in that study was a finite long model including damping. In addition, their study proposed to utilize the embedded piezoelectric element for energy harvesting. Hu *et al.*²⁵ modified the conventional metamaterial (classic mass-in-mass spring system⁵) through introducing internal coupling between local resonators. The internally coupled metamaterial

^{a)}Author to whom correspondence should be addressed: l.tang@auckland.ac.nz

can provide three band gaps for broadband vibration suppression. Zhou *et al.*²⁶ established a metamaterial with a diatomic crystal lattice. They employed and compared several modelling methods for calculating the band structure. Overall, multiple band gaps were observed in the modified metamaterial.

In recent years, the applications of metamaterials have been extended into the field of energy harvesting.^{27–29} Shen *et al.*¹⁰ designed a metamaterial plate consisting of an array of spiral beams as the conversion medium for energy harvesting and claimed that the output power was enhanced at multiple resonant frequencies in the low frequency range. Mikoshiba *et al.*³⁰ proposed an energy harvesting system with a periodic structure embedded with multiple local resonators made of spring-suspended magnets. As aforementioned, Hu *et al.*²⁴ proposed a tunable metamaterial with embedded piezoelectric elements for achieving simultaneous energy harvesting and vibration suppression. A more recent study³¹ extended their work to a piezoelectric metamaterial beam through distributed parameter modelling. They investigated this piezoelectric metamaterial beam from both the vibration suppression and energy harvesting perspectives. A recent review paper on the topic of metamaterial-inspired energy harvesting can be referred to Ref. 32.

On the basis of the models presented in Refs. 25 and 31, this paper proposes an internally coupled metamaterial beam embedded with piezoelectric elements. Such a beam based on the distributed parameter model represents a more practical structure of internally coupled metamaterials. It is explored in this paper that the phenomenon of the appearance of the additional band gap due to the introduction of the internal coupling discovered in Ref. 25 still occurs in the distributed parameter model. As the vibration suppression performance of metamaterials is determined by band gaps, the occurrence of the additional band gap can enhance the vibration suppression ability. In addition, the idea of the piezoelectric metamaterial beam introduced in Ref. 31 for improved simultaneous vibration suppression and energy harvesting is extended in this proposed model. It will be shown that the introduction of the internal coupling could benefit the energy harvesting performance of the proposed system as well. First, based on the Euler-Bernoulli beam theory and the transfer matrix method, the infinite long model of the proposed modified metamaterial beam is developed and its band structure is calculated analytically. The finite long model of the proposed modified metamaterial beam is then also developed and its transmittance is calculated. Predictions of band gaps from the band structure and the transmittance are compared. Subsequently, under weak coupling conditions, by embedding piezoelectric elements with local resonators, the energy

harvesting performance of the system is analytically investigated. In addition to the analytical study, two types of finite element (FE) models (termed models A and B) are established. In Model A, each local oscillator represented by lumped parameters in the analytical model is modelled by using a pair of cantilever beams with tip masses. These tip masses are alternately coupled with ideal springs. In Model B, the ideal spring connection is replaced by a beam connection, which is analogous to a more practical implementation. Both vibration suppression and energy harvesting performances of these two models are analysed and compared. The differences between the FE models and analytical models are discussed.

II. THEORETICAL ANALYSIS

A. Conventional metamaterial beam

This section briefly reviews the methodologies for calculating the band gaps of conventional metamaterial beams. Figure 1(a) shows the infinite long model of a conventional metamaterial beam. Uniform local resonators are periodically attached onto the host plain beam at a constant spacing of d . Each resonator is consisted of a mass m and a linear spring with a constant stiffness of k . Based on the Euler-Bernoulli beam theory and the transfer matrix method, the band structure of this system can be derived.^{12,13,18} Figure 1(b) shows the finite long model of the conventional metamaterial beam. A recent study by Hu *et al.*³¹ presents an analytical study of this kind of system. Adopting the methods proposed by the existing literature, Fig. 2 shows the band structure of an infinite model and the transmittance of a finite long model. The system parameters used in the calculation are listed in Table I.

The band gap signifies a frequency range within which there is no real solution for wave number. From another viewpoint, this implies that for a given wave number, only real solutions of frequency represent the waves which could propagate within the metamaterial. Otherwise, complex solutions represent evanescent waves whose energy quickly decreases with the distance. In the band structure [Fig. 2(a)], the frequency range 89.8–122.1 Hz (blue shaded area) denotes the band gap. The band gap correspondingly exhibits as a valley in the transmittance [Fig. 2(b)]. This is more physically understandable, as in the band gap, vibrations are strongly suppressed, thus resulting in an extremely low transmittance. The blue shaded area in the transmittance marks the band gap range obtained from the band structure. It can be noted that predictions of the band gap from the band structure and transmittance are in good agreement.

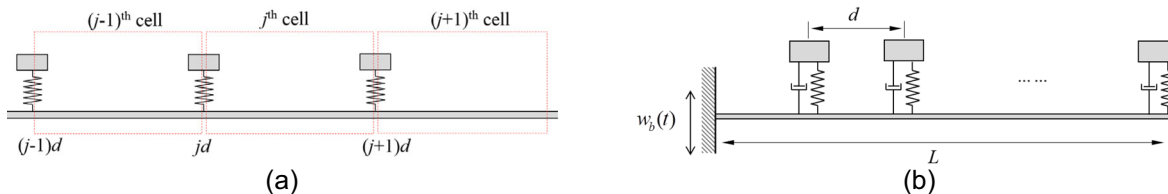


FIG. 1. Conventional metamaterial beam: (a) infinite long model and (b) finite long model.

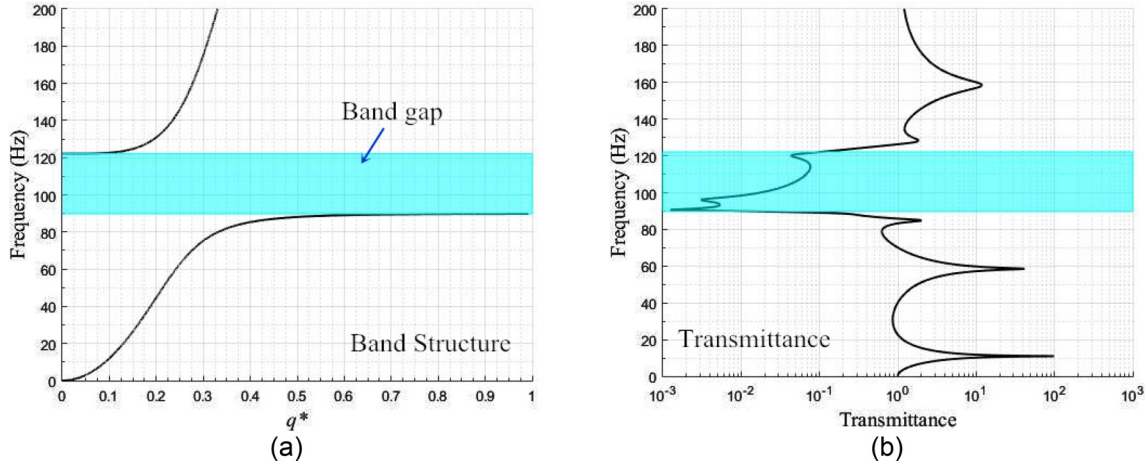


FIG. 2. (a) Band structure and (b) transmittance of the conventional metamaterial beam.

TABLE I. System parameters under investigation.

Parameters	Values
Beam cross-section area A_{cs}	$0.020 \times 0.004 \text{ m}^2$
Beam mass density ρ	7860 m
Young's Modulus E	$200 \times 10^9 \text{ Pa}$
Periodic constant d	0.075 m
Local resonator mass m	0.0396 kg
Local resonator stiffness k	$1.2663 \times 10^4 \text{ N/m}$

B. Vibration suppression of the modified metamaterial beam

This section describes the structure of the modified metamaterial beam and investigates its vibration suppression performance through the band structure of an infinite long model and the transmittance of a finite long model.

1. Band structure

Figure 3 shows the infinite long model of the proposed internally coupled metamaterial beam. Uniform local resonators are periodically attached onto the host plain beam at a constant spacing of d . Each resonator is consisted of a mass m and a linear spring of stiffness k . Different from the conventional metamaterial beam, in the modified one, every two neighbouring local resonators form a new distinct

group and interact with each other through a linear coupling spring k_c .

According to the Euler-Bernoulli beam theory, the governing equation of the beam can be written as

$$EI \frac{\partial^4 w(x, t)}{\partial x^4} + \rho A_{cs} \frac{\partial^2 w(x, t)}{\partial t^2} = 0, \quad (1)$$

where EI , ρ , and A_{cs} are the bending stiffness, density, and cross-section area of the beam, respectively; $w(x, t)$ is the deflection at position x . The solution of $w(x, t)$ is assumed to be in the form of $w(x, t) = W(x)e^{i\omega t}$, where $W(x)$ is the deflection amplitude of the beam and ω is the circular frequency. Since only the steady-state response is of interest, the time factor $e^{i\omega t}$, which applies to all the field variables, can be disregarded. For an Euler-Bernoulli beam, the general solution of the deflection amplitude of the beam $W(x)$ is

$$W(x) = A \cos(\beta x) + B \sin(\beta x) + C \cosh(\beta x) + D \sinh(\beta x), \quad (2)$$

where $\beta^4 = \frac{\rho A_{cs} \omega^2}{EI}$. As each cell is consisted of two subsections, therefore, the deflection amplitudes of the left-hand-side (lhs) and right-hand-side (rhs) subsections of the j th cell of the beam are

$$\begin{cases} W_j^l(x) = \left[A_j^l \cos(\beta(x - j2d)) + B_j^l \sin(\beta(x - j2d)) \right. \\ \quad \left. + C_j^l \cosh(\beta(x - j2d)) + D_j^l \sinh(\beta(x - j2d)) \right] \\ W_j^r(x) = \left[A_j^r \cos(\beta(x - j2d - d)) + B_j^r \sin(\beta(x - j2d - d)) \right. \\ \quad \left. + C_j^r \cosh(\beta(x - j2d - d)) + D_j^r \sinh(\beta(x - j2d - d)) \right]. \end{cases} \quad (3)$$

The equations of motion of the left and right resonators in the j th cell are

$$\begin{cases} m \ddot{u}_j^l(t) + k_c(u_j^l(t) - u_j^r(t)) + k(u_j^l(t) - w_j^l(j2d, t)) = 0 \\ m \ddot{u}_j^r(t) + k_c(u_j^r(t) - u_j^l(t)) + k(u_j^r(t) - w_j^r(j2d + d, t)) = 0, \end{cases} \quad (4)$$

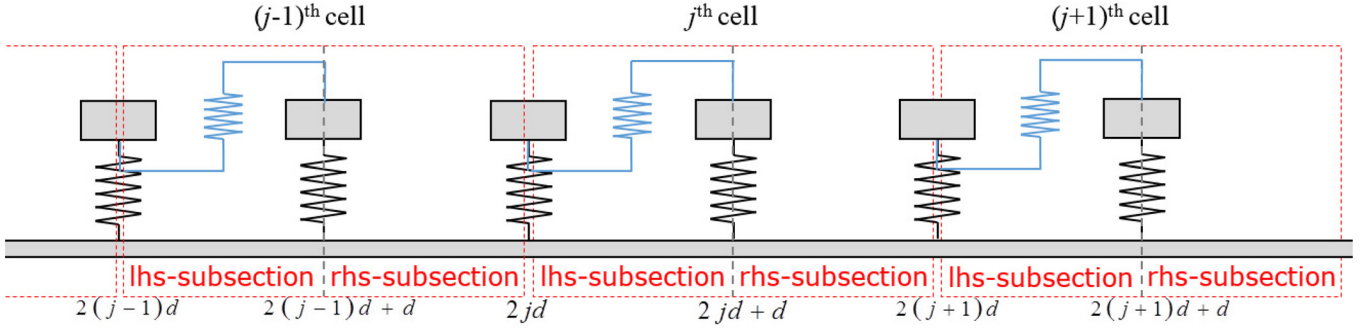


FIG. 3. Infinite long model of the internally coupled metamaterial beam.

where k_c is the stiffness of the coupling spring; and u_j^l and u_j^r are the absolute displacements of the left and right local resonators, respectively. The reaction forces of the left and right local resonators in the j th cell acting on the plain beam can be calculated as

$$\begin{cases} F_j^l = k(W_j^l(j2d) - U_j^l) \\ F_j^r = k(W_j^r(j2d + d) - U_j^r). \end{cases} \quad (5)$$

Solving Eq. (4) to represent the magnitudes of oscillators U_j^l and U_j^r in terms of W_j^l and W_j^r , and substituting them into Eq. (5) gives

$$\begin{cases} F_j^l = aW_j^l(j2d) - bW_j^r(j2d + d) \\ F_j^r = -bW_j^l(j2d) + aW_j^r(j2d + d), \end{cases} \quad (6)$$

where $a = k(1 - \frac{(k_c+k-m\omega^2)k}{(k_c+k-m\omega^2)^2-k_c^2})$, $b = \frac{k^2k_c}{(k_c+k-m\omega^2)^2-k_c^2}$.

Applying the continuity conditions of deflection, slope, bending moment, and shear force at the interface between

the left and the right subsections of the beam in the $(j-1)$ th cell, we have

$$\begin{cases} W_{j-1}^r(j2d - d) = W_{j-1}^l(j2d - d) \\ \frac{\partial W_{j-1}^r(j2d - d)}{\partial x} = \frac{\partial W_{j-1}^l(j2d - d)}{\partial x} \\ EI \frac{\partial^2 W_{j-1}^r(j2d - d)}{\partial x^2} = EI \frac{\partial^2 W_{j-1}^l(j2d - d)}{\partial x^2} \\ EI \frac{\partial^3 W_{j-1}^r(j2d - d)}{\partial x^3} + F_{j-1}^r = EI \frac{\partial^3 W_{j-1}^l(j2d - d)}{\partial x^3}. \end{cases} \quad (7)$$

Substituting Eqs. (3) and (6) into Eq. (7), we can express the continuity conditions in the matrix form as

$$\mathbf{K}\Psi_{j-1}^r = \mathbf{H}\Psi_{j-1}^l, \quad (8)$$

where

$$\mathbf{K} = \begin{bmatrix} 1 & 0 & 1 & 0 \\ 0 & 1 & 0 & 1 \\ -1 & 0 & 1 & 0 \\ \frac{a}{\beta^3 EI} & -1 & \frac{a}{\beta^3 EI} & 1 \end{bmatrix}, \quad \mathbf{H} = \begin{bmatrix} \cos(\beta d) & \sin(\beta d) & \cosh(\beta d) & \sinh(\beta d) \\ -\sin(\beta d) & \cos(\beta d) & \sinh(\beta d) & \cosh(\beta d) \\ -\cos(\beta d) & -\sin(\beta d) & \cosh(\beta d) & \sinh(\beta d) \\ \left(\sin(\beta d) + \frac{b}{\beta^3 EI}\right) & -\cos(\beta d) & \left(\sinh(\beta d) + \frac{b}{\beta^3 EI}\right) & \cosh(\beta d) \end{bmatrix},$$

$$\Psi_{j-1}^r = [A_{j-1}^r \quad B_{j-1}^r \quad C_{j-1}^r \quad D_{j-1}^r]^T, \quad \Psi_{j-1}^l = [A_{j-1}^l \quad B_{j-1}^l \quad C_{j-1}^l \quad D_{j-1}^l]^T.$$

Similarly, applying the continuity conditions of deflection, slope, bending moment, and shear force at the interface between the $(j-1)$ th cell and the j th cell, we have

$$\begin{cases} W_j^l(j2d) = W_{j-1}^r(j2d) \\ \frac{\partial W_j^l(j2d)}{\partial x} = \frac{\partial W_{j-1}^r(j2d)}{\partial x} \\ EI \frac{\partial^2 W_j^l(j2d)}{\partial x^2} = EI \frac{\partial^2 W_{j-1}^r(j2d)}{\partial x^2} \\ EI \frac{\partial^3 W_j^l(j2d)}{\partial x^3} + F_j^l = EI \frac{\partial^3 W_{j-1}^r(j2d)}{\partial x^3}. \end{cases} \quad (9)$$

Substituting Eqs. (3) and (6) into Eq. (9), we can express the continuity conditions in the matrix form as

$$\mathbf{A}\Psi_j^l + \mathbf{B}\Psi_j^r = \mathbf{H}'\Psi_{j-1}^r, \quad (10)$$

where

$$\mathbf{A} = \begin{bmatrix} 1 & 0 & 1 & 0 \\ 0 & 1 & 0 & 1 \\ -1 & 0 & 1 & 0 \\ \frac{a}{\beta^3 EI} & -1 & \frac{a}{\beta^3 EI} & 1 \end{bmatrix},$$

$$\mathbf{B} = \begin{bmatrix} 0 & 0 & 0 & 0 \\ 0 & 0 & 0 & 0 \\ 0 & 0 & 0 & 0 \\ -\frac{b}{\beta^3 EI} & 0 & -\frac{b}{\beta^3 EI} & 0 \end{bmatrix},$$

$$\mathbf{H}' = \begin{bmatrix} \cos(\beta d) & \sin(\beta d) & \cosh(\beta d) & \sinh(\beta d) \\ -\sin(\beta d) & \cos(\beta d) & \sinh(\beta d) & \cosh(\beta d) \\ -\cos(\beta d) & -\sin(\beta d) & \cosh(\beta d) & \sinh(\beta d) \\ \sin(\beta d) & -\cos(\beta d) & \sinh(\beta d) & \cosh(\beta d) \end{bmatrix},$$

$$\Psi_j^l = [A_j^l \ B_j^l \ C_j^l \ D_j^l],$$

$$\Psi_{j-1}^r = [A_{j-1}^r \ B_{j-1}^r \ C_{j-1}^r \ D_{j-1}^r].$$

Combining Eqs. (8) and (10) and eliminating Ψ_{j-1}^r and Ψ_j^r , we can obtain the transfer matrix between the two cells

$$\Psi_j^l = \underbrace{(\mathbf{A} + \mathbf{B}\mathbf{K}^{-1}\mathbf{H})^{-1}\mathbf{H}'(\mathbf{K})^{-1}\mathbf{H}}_{\mathbf{T}}\Psi_{j-1}^r. \quad (11)$$

According to the Bloch theorem, the periodicity condition yields

$$\Psi_j^l = e^{iq2d}\Psi_{j-1}^l, \quad (12)$$

where q is the wavenumber. Inserting Eq. (11) into Eq. (12), a standard eigenvalue problem is formed

$$|\mathbf{T} - e^{iq2d}\mathbf{I}| = 0, \quad (13)$$

where \mathbf{I} is the 4-order unit matrix.

For the given system parameters listed in Table I, Fig. 4 shows the band structures of the modified metamaterial beam for different values of the coupling spring stiffness.

It can be noted that in the modified metamaterial beam, two band gaps appear due to the existence of the internal coupling. For Figs. 4(a)–4(d), the first band gap ranges

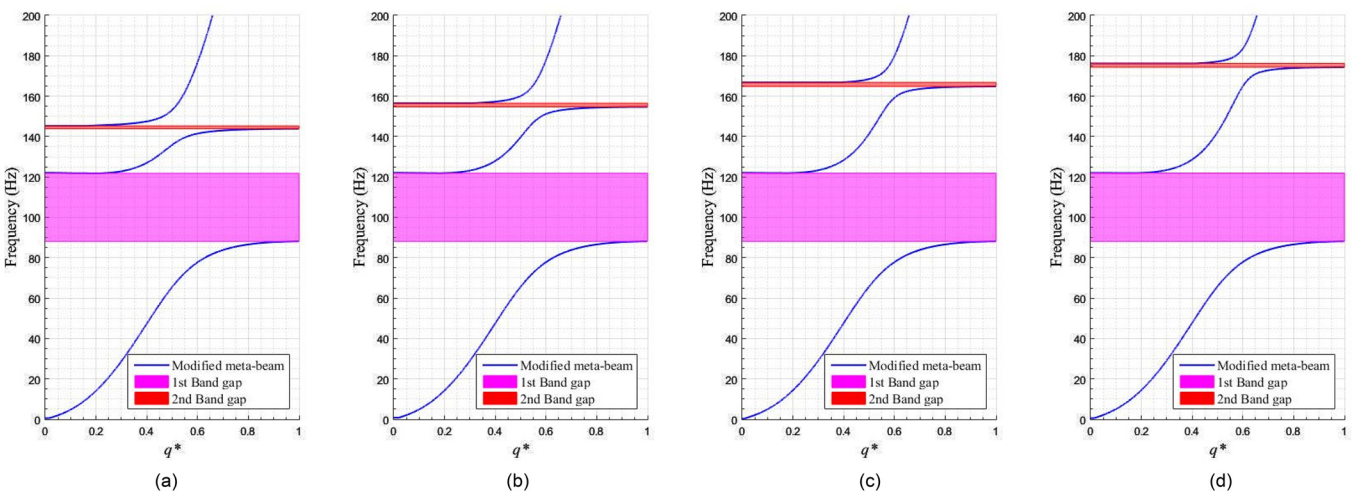


FIG. 4. Band structure of the internally coupled metamaterial beam: (a) $k_c=0.8k$; (b) $k_c=1.0k$; (c) $k_c=1.2k$; and (d) $k_c=1.4k$.

are (88.1–121.9 Hz), (88.1–121.9 Hz), (88.1–121.9 Hz), and (88.1–121.9 Hz), respectively. The second band gap ranges are (143.9–145.3 Hz), (154.7–156.5 Hz), (164.8–166.4 Hz), and (174.3–176.2 Hz), respectively. Comparing Figs. 4(a) and 2(a), the first band gap (the purple shaded area) almost coincides with that of the conventional metamaterial beam. An additional second narrow band gap (the red shaded area) appears in a slight higher frequency range. In addition, comparing Figs. 4(a)–4(d), it is found that with the increase of the coupling spring stiffness k_c , the first band gap is unaffected. The location of the second band gap moves toward a higher frequency and the width of the second band gap varies. However, since the second band gap is very narrow as compared to the first band gap, no matter how its width increases or decreases, its variation is not noticeable.

2. Transmittance

This section investigates a more practical finite long model with a certain energy dissipation mechanism of the proposed internally coupled metamaterial beam as shown in Fig. 5. The host plain beam is of length L . $2S$ resonators are periodically placed onto the host beam at a uniform distance of d . The left-hand side of the beam is clamped on a base that experiences a harmonic excitation $w_b(t) = W_b e^{i\omega t}$. The acceleration of the base excitation is controlled at a constant acceleration $a_{cc} = -\omega^2 W_b$. By adopting the Euler-Bernoulli beam theory, the governing equation of the metamaterial beam is written as

$$\begin{aligned} EI \frac{\partial^4 w_{rel}(x, t)}{\partial x^4} + c_s I \frac{\partial^5 w_{rel}(x, t)}{\partial x^4 \partial t} + \rho A_{cs} \frac{\partial^2 w_{rel}(x, t)}{\partial t^2} \\ = \rho A_{cs} a_{cc} e^{i\omega t} - \sum_{j=1}^S \left[F_j^l \delta(x - x_j^l) + F_j^r \delta(x - x_j^r) \right] e^{i\omega t}, \end{aligned} \quad (14)$$

where $w_{rel}(x, t)$ is the relative transverse displacement between the beam $w(x, t)$ and the base $w_b(t)$, i.e., $w_{rel}(x, t) = w(x, t) - w_b(t)$; c_s is the equivalent strain rate damping

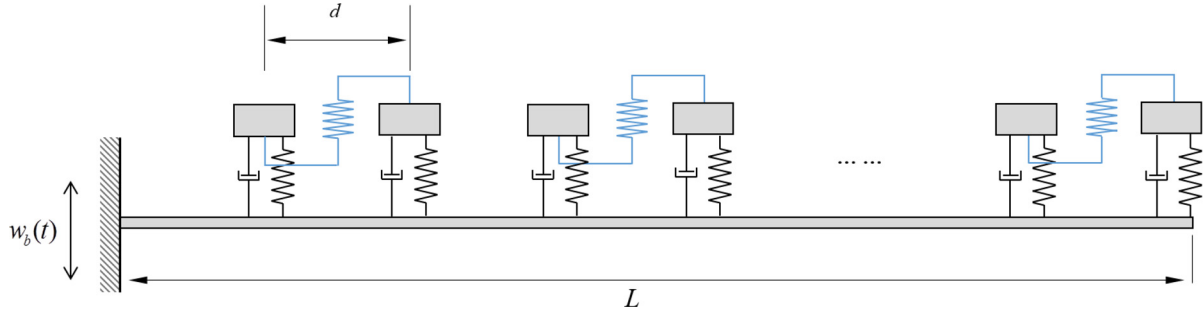


FIG. 5. Finite long model of the internally coupled metamaterial beam.

constant; F_j^l and F_j^r are the total reaction forces exerted by the left and right oscillators in the j th cell onto the beam during vibration, respectively; and $\delta(x)$ is the Dirac delta function. The equations of motion for oscillators are

$$\begin{cases} m\ddot{u}_j^l(t) + c\dot{u}_j^l(t) + ku_j^l(t) + k_c(u_j^l(t) + w(x_j^l, t) - u_j^r(t) - w(x_j^r, t)) = -m\ddot{w}(x_j^l, t) \\ m\ddot{u}_j^r(t) + c\dot{u}_j^r(t) + ku_j^r(t) + k_c(u_j^r(t) + w(x_j^r, t) - u_j^l(t) - w(x_j^l, t)) = -m\ddot{w}(x_j^r, t), \end{cases} \quad (15)$$

where $u_j^l(t)$ and $u_j^r(t)$ are the displacements of the left and right oscillator masses in the j th cell relative to the host beam, respectively. The absolute displacement of the oscillator mass should add $w(x_j, t)$.

Using the modal superposition method, the relative displacement along the beam can be written as

$$w_{rel}(x, t) = \sum_{k=1}^{\infty} \phi_k(x) \eta_k(t) \quad (k = 1, 2, 3\dots), \quad (16)$$

where functions $\phi_k(x)$ are the normalized mode shape functions of the plain beam (i.e., without oscillators) and functions $\eta_k(t)$ are the modal coordinates. Substituting Eq. (16) into (14), multiplying by $\phi_n(x)$, and integrating over the beam length from 0 to L , then using the orthogonal conditions ($\int_0^L \rho A_{cs} \phi_r(x) \phi_j(x) dx = \delta_{rj}$, $\int_0^L EI \frac{d^4 \phi_r(x)}{dx^4} \phi_j(x) dx = \omega_r^2 \delta_{rj}$), we obtain the modal governing equation as

$$\ddot{\eta}_n(t) + 2\zeta_n \omega_n \dot{\eta}_n(t) + \omega_n^2 \eta_n(t) = \rho A_{cs} a_{cc} e^{i\omega t} \int_0^L \phi_n(x) dx - \sum_{j=1}^S [F_j^l \phi_n(x_j^l) e^{i\omega t} + F_j^r \phi_n(x_j^r) e^{i\omega t}], \quad (17)$$

where $\zeta_n = \frac{c I \omega_n}{2 E}$. The expression of $\eta_n(t)$ can be derived from Eq. (17). Substituting the derived $\eta_n(t)$ into Eq. (16) provides the closed-form solution of the relative displacement as

$$w_{rel}(x, t) = \sum_{k=1}^{\infty} \phi_k(x) \frac{\rho A_{cs} a_{cc} \int_0^L \phi_k(x) dx - \sum_{j=1}^S [F_j^l \phi_k(x_j^l) + F_j^r \phi_k(x_j^r)]}{\omega_k^2 - \omega^2 + 2i\zeta_k \omega_k \omega} e^{i\omega t}. \quad (18)$$

From Eq. (15), we can obtain

$$\begin{cases} u_j^l(t) = \alpha_1 w_{rel}(x_j^l) + \alpha_2 w_{rel}(x_j^r) + \alpha_3 w_b(t) \\ u_j^r(t) = \alpha_2 w_{rel}(x_j^l) + \alpha_1 w_{rel}(x_j^r) + \alpha_3 w_b(t), \end{cases} \quad (19)$$

where

$$\begin{cases} \alpha_1 = \frac{[k_c^2 - (k_c - m\omega^2)(k + k_c - m\omega^2 + i\omega c)]}{(k + k_c - m\omega^2 + i\omega c)^2 - k_c^2} \\ \alpha_2 = \frac{k_c(k + i\omega c)}{(k + k_c - m\omega^2 + i\omega c)^2 - k_c^2} \\ \alpha_3 = \frac{[k_c^2 - (k_c - m\omega^2)(k + k_c - m\omega^2 + i\omega c)] + k_c(k + i\omega c)}{(k + k_c - m\omega^2 + i\omega c)^2 - k_c^2}. \end{cases}$$

The reaction forces exerted by the left and right oscillators in the j th cell onto the beam are expressed as

$$\begin{cases} f_j^l = -[cu_j^l(t) + ku_j^l(t)] = -(k + i\omega c)\alpha_1 w_{rel}(x_j^l) + \alpha_2 w_{rel}(x_j^r) + \alpha_3 w_b(t) \\ f_j^r = -[c\dot{u}_j^r(t) + ku_j^r(t)] = -(k + i\omega c)\alpha_2 w_{rel}(x_j^l) + \alpha_1 w_{rel}(x_j^r) + \alpha_3 w_b(t). \end{cases} \quad (20)$$

Substituting Eq. (18) into Eq. (20) gives the expression of the force amplitude as

$$\left\{ \begin{array}{l} F_j^l = -(k + i\omega c) \left\{ \begin{array}{l} \alpha_1 \times \sum_{k=1}^{\infty} \phi_k(x_j^l) \frac{\rho A_{cs} a_{cc} \int_0^L \phi_k(x) dx - \sum_{h=1}^S [F_h^l \phi_k(x_h^l) + F_h^r \phi_k(x_h^r)]}{\omega_k^2 - \omega^2 + 2i\zeta_k \omega_k \omega} \\ + \alpha_2 \times \sum_{k=1}^{\infty} \phi_k(x_j^r) \frac{\rho A_{cs} a_{cc} \int_0^L \phi_k(x) dx - \sum_{h=1}^S [F_h^l \phi_k(x_h^l) + F_h^r \phi_k(x_h^r)]}{\omega_k^2 - \omega^2 + 2i\zeta_k \omega_k \omega} + \alpha_3 \frac{a_{cc}}{\omega^2} \end{array} \right\} \\ F_j^r = -(k + i\omega c) \left\{ \begin{array}{l} \alpha_2 \times \sum_{k=1}^{\infty} \phi_k(x_j^l) \frac{\rho A_{cs} a_{cc} \int_0^L \phi_k(x) dx - \sum_{h=1}^S [F_h^l \phi_k(x_h^l) + F_h^r \phi_k(x_h^r)]}{\omega_k^2 - \omega^2 + 2i\zeta_k \omega_k \omega} \\ + \alpha_1 \times \sum_{k=1}^{\infty} \phi_k(x_j^r) \frac{\rho A_{cs} a_{cc} \int_0^L \phi_k(x) dx - \sum_{h=1}^S [F_h^l \phi_k(x_h^l) + F_h^r \phi_k(x_h^r)]}{\omega_k^2 - \omega^2 + 2i\zeta_k \omega_k \omega} + \alpha_3 \frac{a_{cc}}{\omega^2} \end{array} \right\}. \end{array} \right. \quad (21)$$

Rearrange the $2S$ reaction force equations, i.e., $F_1^l, F_2^l, \dots, F_S^l, F_1^r, F_2^r, \dots, F_S^r$

$$\left\{ \begin{array}{l} a_{1,1}F_1^l + a_{1,2}F_2^l + \dots + a_{1,S}F_S^l + a_{1,S+1}F_1^r + a_{1,S+2}F_2^r + \dots + a_{1,2S}F_S^r = b_1 \\ \dots \\ a_{j,1}F_1^l + a_{j,2}F_2^l + \dots + a_{j,S}F_S^l + a_{j,S+1}F_1^r + a_{j,S+2}F_2^r + \dots + a_{j,2S}F_S^r = b_j \\ \dots \\ a_{S,1}F_1^l + a_{S,2}F_2^l + \dots + a_{S,S}F_S^l + a_{S,S+1}F_1^r + a_{S,S+2}F_2^r + \dots + a_{S,2S}F_S^r = b_S \\ a_{S+1,1}F_1^l + a_{S+1,2}F_2^l + \dots + a_{S+1,S}F_S^l + a_{S+1,S+1}F_1^r + a_{S+1,S+2}F_2^r + \dots + a_{S+1,2S}F_S^r = b_{S+1} \\ \dots \\ a_{S+j,1}F_1^l + a_{S+j,2}F_2^l + \dots + a_{S+j,S}F_S^l + a_{S+j,S+1}F_1^r + a_{S+j,S+2}F_2^r + \dots + a_{S+j,2S}F_S^r = b_{S+j} \\ \dots \\ a_{2S,1}F_1^l + a_{2S,2}F_2^l + \dots + a_{2S,S}F_S^l + a_{2S,S+1}F_1^r + a_{2S,S+2}F_2^r + \dots + a_{2S,2S}F_S^r = b_{2S}, \end{array} \right. \quad (22)$$

where

$$a_{j,h} = \left\{ \begin{array}{l} \left(\alpha_1 \times \sum_{k=1}^{\infty} \frac{\phi_k(x_j^l) \phi_k(x_h^l)}{\omega_k^2 - \omega^2 + 2i\zeta_k \omega_k \omega} + \alpha_2 \times \sum_{k=1}^{\infty} \frac{\phi_k(x_j^r) \phi_k(x_h^l)}{\omega_k^2 - \omega^2 + 2i\zeta_k \omega_k \omega} \right) \quad \text{for } 1 \leq j \leq S; 1 \leq h \leq S \\ \left(\alpha_1 \times \sum_{k=1}^{\infty} \frac{\phi_k(x_j^l) \phi_k(x_{(h-S)}^r)}{\omega_k^2 - \omega^2 + 2i\zeta_k \omega_k \omega} + \alpha_2 \times \sum_{k=1}^{\infty} \frac{\phi_k(x_j^r) \phi_k(x_{(h-S)}^r)}{\omega_k^2 - \omega^2 + 2i\zeta_k \omega_k \omega} \right) \quad \text{for } 1 \leq j \leq S; S+1 \leq h \leq 2S \\ \left(\alpha_2 \times \sum_{k=1}^{\infty} \frac{\phi_k(x_{(j-S)}^l) \phi_k(x_h^l)}{\omega_k^2 - \omega^2 + 2i\zeta_k \omega_k \omega} + \alpha_1 \times \sum_{k=1}^{\infty} \frac{\phi_k(x_{(j-S)}^r) \phi_k(x_h^l)}{\omega_k^2 - \omega^2 + 2i\zeta_k \omega_k \omega} \right) \quad \text{for } S+1 \leq j \leq 2S; 1 \leq h \leq S \\ \left(\alpha_2 \times \sum_{k=1}^{\infty} \frac{\phi_k(x_{(j-S)}^l) \phi_k(x_{(h-S)}^r)}{\omega_k^2 - \omega^2 + 2i\zeta_k \omega_k \omega} + \alpha_1 \times \sum_{k=1}^{\infty} \frac{\phi_k(x_{(j-S)}^r) \phi_k(x_{(h-S)}^r)}{\omega_k^2 - \omega^2 + 2i\zeta_k \omega_k \omega} \right) \quad \text{for } S+1 \leq j \leq 2S; S+1 \leq h \leq 2S, \end{array} \right.$$

$$a_{jj} = \begin{cases} \left(\alpha_1 \times \sum_{k=1}^{\infty} \frac{\phi_k(x_j^l) \phi_k(x_j^r)}{\omega_k^2 - \omega^2 + 2i\zeta_k \omega_k \omega} + \alpha_2 \times \sum_{k=1}^{\infty} \frac{\phi_k(x_j^r) \phi_k(x_j^l)}{\omega_k^2 - \omega^2 + 2i\zeta_k \omega_k \omega} - \frac{1}{(k+i\omega c)} \right) & \text{for } 1 \leq j \leq S \\ \left(\alpha_2 \times \sum_{k=1}^{\infty} \frac{\phi_k(x_{(j-S)}^l) \phi_k(x_{(j-S)}^r)}{\omega_k^2 - \omega^2 + 2i\zeta_k \omega_k \omega} + \alpha_1 \times \sum_{k=1}^{\infty} \frac{\phi_k(x_{(j-S)}^r) \phi_k(x_{(j-S)}^l)}{\omega_k^2 - \omega^2 + 2i\zeta_k \omega_k \omega} - \frac{1}{(k+i\omega c)} \right) & \text{for } S+1 \leq j \leq 2S, \end{cases}$$

$$b_j = \begin{cases} \left(\alpha_1 \times \sum_{k=1}^{\infty} \phi_k(x_j^l) \frac{\rho A_{cs} a_{cc}}{\omega_k^2 - \omega^2 + 2i\zeta_k \omega_k \omega} \int_0^L \phi_k(x) dx + \alpha_2 \times \sum_{k=1}^{\infty} \phi_k(x_j^r) \frac{\rho A_{cs} a_{cc}}{\omega_k^2 - \omega^2 + 2i\zeta_k \omega_k \omega} \int_0^L \phi_k(x) dx + \alpha_3 \frac{a_{cc}}{\omega^2} \right) & \text{for } 1 \leq j \leq S \\ \left(\alpha_2 \times \sum_{k=1}^{\infty} \phi_k(x_{(j-S)}^l) \frac{\rho A_{cs} a_{cc}}{\omega_k^2 - \omega^2 + 2i\zeta_k \omega_k \omega} \int_0^L \phi_k(x) dx + \alpha_1 \times \sum_{k=1}^{\infty} \phi_k(x_{(j-S)}^r) \frac{\rho A_{cs} a_{cc}}{\omega_k^2 - \omega^2 + 2i\zeta_k \omega_k \omega} \int_0^L \phi_k(x) dx + \alpha_3 \frac{a_{cc}}{\omega^2} \right) & \text{for } S+1 \leq j \leq 2S. \end{cases}$$

By solving Eq. (22), the $2S$ values of F_j^l and F_j^r can be calculated. Substituting them back into Eq. (18), the relative deflection amplitude $W_{rel}(x)$ can be obtained. The transmittance of the system is defined and calculated as

$$\tau = \frac{|W_{rel}(L) + W_b|}{|W_b|}. \quad (23)$$

With the parameters listed in Table I, the transmittances of the modified metamaterial beam are calculated for different values of the coupling spring stiffness, as shown in Fig. 6. It is worth noting that the model is now assumed to be finite long, and the supplementary information used in the calculation includes—material damping ratio 0.009; oscillator damping ratio 0.009; and beam length 0.45 m (thus there are 6 local resonators attached onto the beam). The colour shaded areas are band gaps predicted by the band structure from Sec. II B 1 (Fig. 4) and are replotted in Fig. 6. As predicted in the band structure, the modified metamaterial beam inherits the band gap of the conventional one and provides an additional second band gap in a higher frequency range. Figure 6 clearly shows that both the band structure and the transmittance well predict the existence and the range of band gaps and they are in good agreement with each other.

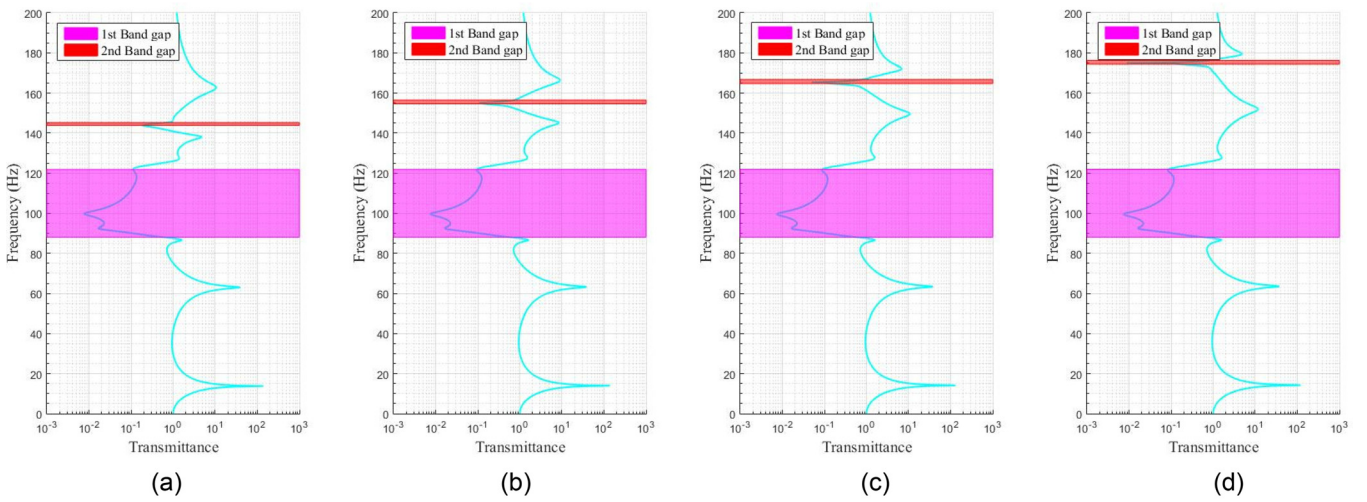


FIG. 6. Transmittance of the internally coupled metamaterial beam: (a) $k_c=0.8k$; (b) $k_c=1.0k$; (c) $k_c=1.2k$; and (d) $k_c=1.4k$.

C. Energy harvesting of the modified metamaterial beam

Hu *et al.*²⁴ integrated local resonators with piezoelectric elements and proposed a metamaterial based energy harvester which was modelled with lumped parameters. However, in reality, lumped parameter models sometimes cannot well predict the behaviour of physically distributed parameter systems. Naturally, this concept can be easily extended by using distributed parameter modelling which yields a metamaterial beam based piezoelectric energy harvester (PEH).³¹ In addition, we modify the piezoelectric metamaterial beam by introducing the internal coupling of local resonators. In this section, the energy harvesting performance of this modified beam is analytically studied and compared with that of the conventional piezoelectric metamaterial beam in Ref. 31.

The governing equation of the circuit part is

$$\frac{v}{R} + C^S \dot{v} - \theta \dot{u} = 0, \quad (24)$$

where θ is the electromechanical coupling coefficient; C^S is the clamped capacitance of the piezoelectric element; R is the resistance of the electric resistor connected to the piezoelectric element; v is the voltage across the electric resistor

R ; and u is the relative displacement of the local resonator mass to the beam.

Applying the Laplace transform, we can represent the voltage amplitude by using the amplitude of u

$$|V| = \left| \frac{i\theta\omega U}{\frac{1}{R} + i\omega C^S} \right|. \quad (25)$$

From Eq. (25), by finding the limit of $|V|$ as R approaches positive infinity, the open-circuit voltage amplitude can be expressed as

$$|V_{oc}| = \left| \frac{\theta U}{C^S} \right|. \quad (26)$$

It can be shown that the open-circuit voltage amplitude is linearly proportional to the relative displacement amplitude Y of the local resonator mass, i.e., $|V_{oc}| \propto |U|$. In the following study of energy harvesting performance, the same system previously used with parameters listed in Table I for calculating the transmittances is re-used. The internal coupling spring stiffness is $k_c = 13\,824\text{ N/m}$. The electromechanical coupling coefficient θ and the clamped capacitance C^S are $1.45 \times 10^{-3}\text{ N/V}$ and 18 nF , respectively. In addition, for

consistent comparison, it is assumed that the same piezoelectric elements are used in both the conventional and modified metamaterial beam PEHs.

The base excitation is kept at a constant acceleration $a_{cc} = -1\text{ m/s}^2$. Figures 7(a) and 7(b) show the open circuit voltage responses from the piezoelectric elements in the conventional and the modified metamaterial beam, respectively. It should be noted that the amplitude of the first peak in $|V_{oc}|$ response of the modified metamaterial beam is larger than that of the conventional one for about an order of magnitude. Figures 7(c) and 7(d) show the first peak responses in Figs. 7(a) and 7(b) with a higher frequency resolution. In the conventional metamaterial beam, the piezoelectric element attached to the 6th local resonator (at the tip of the metamaterial beam) exhibits the largest $|V_{oc}|$ equal to 30.7 V at 10.95 Hz . This can be easily explained by the mechanism of the dynamic amplifier.³³ The host beam serves as a dynamic amplifier for those local resonators. Naturally, the tip of the host beam undergoes the most violent motion; thus the local resonator at the utmost tip of the beam gains the largest dynamic amplification. However, after introducing internal coupling, the system's behaviour changes. The 5th local resonator experiences the most significant dynamic amplification at 14.06 Hz and provides a maximum $|V_{oc}|$ equal to 137.6 V . According to Eq. (26), it can be quantitatively

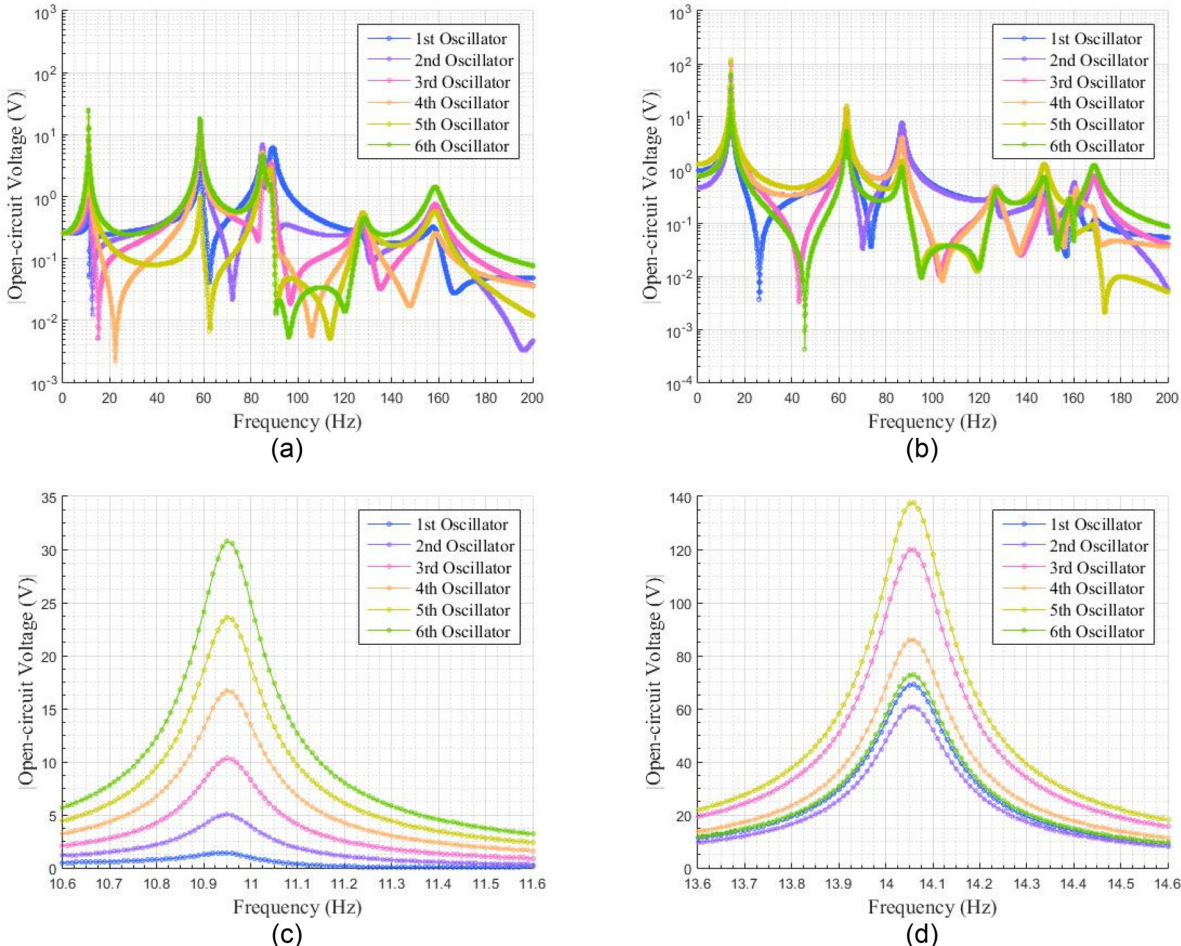


FIG. 7. Open circuit voltage responses of piezoelectric elements embedded in: (a) conventional metamaterial beam and (b) internally coupled metamaterial beam; open circuit voltage responses around first resonance with a higher resolution: (c) conventional metamaterial beam and (d) internally coupled metamaterial beam.

estimated that the maximum $|V_{oc}|$ of the modified metamaterial beam PEH is about 4.5 times that of the conventional one. Therefore, in terms of energy harvesting, the introduction of the internal coupling can significantly enhance the energy harvesting performance.

III. FINITE ELEMENT ANALYSIS

A. Conventional piezoelectric metamaterial beam

Finite element models were developed using the commercial software ANSYS to investigate the performance of the modified metamaterial beam based PEH. The conventional metamaterial beam based PEH was also modelled [Fig. 8(a)] and analysed for comparison. In the finite element model, each lumped local resonator was modelled by a pair of cantilevers with tip masses. Hereinafter, they are referred to as the parasitic beams. They were symmetrically placed at both sides of the host beam. This aims to avoid torsional motion of the host beam caused by imbalance. The six pairs of parasitic beams from the clamped end to the free end are numbered successively as the 1st oscillator to the 6th oscillator. The dynamic behaviour around the fundamental resonance of a cantilever beam with a tip mass can be approximated by a single-degree-of-freedom (DOF) mass-spring oscillator.

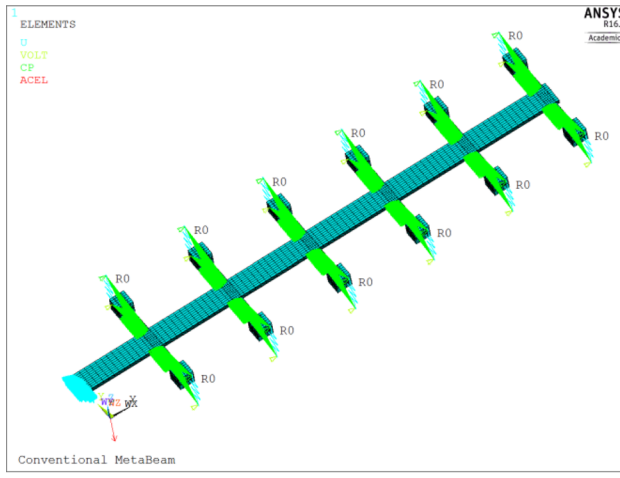
The piezoelectric element was bonded onto the parasitic beam. A three-dimensional (3D) 20-node structural solid element (SOLID186 in ANSYS) was used for the beams and tip masses and a 3D 20-node coupled-field solid element (SOLID226 in ANSYS) was used for the piezoelectric element. Figure 8(b) shows the finite element implementation of the electrode connection of the piezoelectric element bonded onto the parasitic beam. The voltage degrees of freedom (DOFs) on the top and bottom surfaces were coupled to provide uniform electrical potentials and thus to emulate the electrodes. Then, the two electrodes were connected to the resistor by coupling the voltage DOFs of the electrodes and the two nodes of the resistor element. An acceleration field ($a_{cc} = -1 \text{ m/s}^2$) was applied to the system. A harmonic

analysis was performed to obtain steady-state displacement and voltage outputs. It is worth noting that the deflection obtained by applying an acceleration field is the displacement relative to the base. The absolute deflection at the tip of the beam and thus the transmittance is calculated as

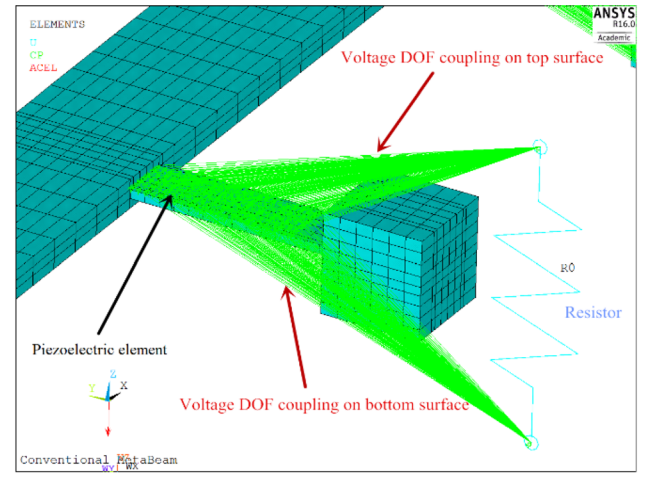
$$\tau = \frac{\left| W_{rel}(L) - \frac{a_{cc}}{\omega^2} \right|}{\left| \frac{a_{cc}}{\omega^2} \right|}. \quad (27)$$

Figure 9(a) shows the transmittance of the conventional metamaterial beam using the finite element method. The band gap is estimated to be (85.9–121.7 Hz) from the FE obtained transmittance. The geometry and material parameters used in the analysis are listed in Table II. It is worth noting that the first natural frequency of the parasitic beam with a tip mass is tuned close to 90 Hz, which is the natural frequency of the local resonator in the spring-mass lumped parameter model. In addition, it is noted that the analytical transmittance curve matches well with the FEA one before the band gap but deviates significantly after the band gap. It has been checked that using 6 modes in the analytical calculation is sufficient to guarantee the convergence, as shown in Fig. 9(b). This deviation comes from the increasing difference between the behaviours of the lumped model and the cantilever with the tip mass model for the local resonator when the frequency increases beyond 100 Hz.

Figure 10(a) shows the open circuit voltage responses of the piezoelectric element bonded onto those 6 parasitic beams over the whole frequency range. From Fig. 10(a), we can identify that the first peak has the largest amplitude (with a low frequency resolution). With a higher frequency resolution, Fig. 10(b) shows the open circuit voltage responses around the first peak. It can be found that the maximum open circuit voltage amplitude is 20.54 V at 11 Hz. Figure 10(c) shows the steady state open circuit voltage contour at the first peak. The contour plot shows that the piezoelectric element embedded with the parasitic beam at the utmost tip of the host beam generates the largest open-circuit



(a)



(b)

FIG. 8. (a) Finite element model of the conventional metamaterial beam embedded with piezoelectric elements and (b) implementation of electrode connection of the piezoelectric element.

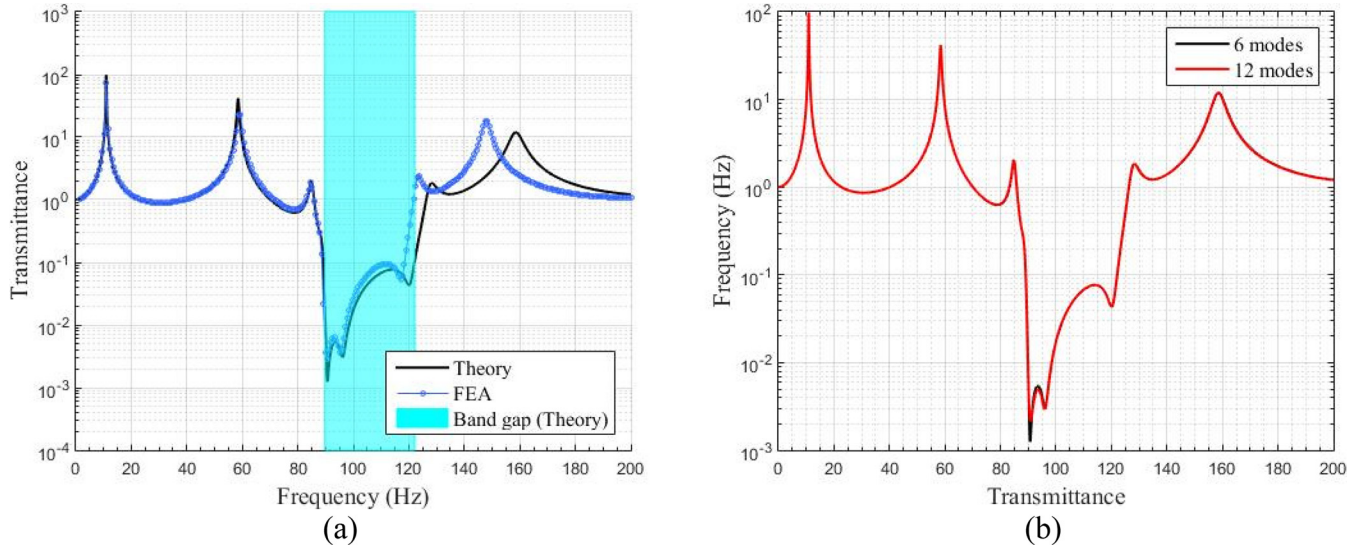


FIG. 9. (a) Comparison of transmittance of the conventional metamaterial beam by finite element analysis and theory and (b) transmittances calculated by using 6 modes and 12 modes.

TABLE II. Physical and geometric properties used in the FE model.

Geometry parameters		Material parameters	
Host beam length	0.45 m	Host beam material density	7860 kg/m^3
Host beam width	0.020 m	Host beam Young's modulus	$200 \times 10^9 \text{ Pa}$
Host beam thickness	0.004 m	Parasitic beam material density	2700 kg/m^3
Parasitic beam length	0.0282 m	Parasitic beam Young's modulus	$69.5 \times 10^9 \text{ Pa}$
Parasitic beam width	0.0078 m	Tip mass material density	7860 kg/m^3
Parasitic beam thickness	0.0012 m	Tip mass Young's modulus	$200 \times 10^9 \text{ Pa}$
Tip mass length	0.0136 m	Piezoelectric material density	5440 kg/m^3
Tip mass width	0.0136 m	Piezoelectric material Young's modulus	$30.336 \times 10^9 \text{ Pa}$
Tip mass thickness	0.0136 m	Strain coefficient of the piezoelectric layer	-170 pC/N
Piezoelectric layer length	0.022 m	Permittivity component at constant strain	$1.3281 \times 10^{-8} \text{ F/m}$
Piezoelectric layer width	0.0062 m	Global damping ratio	0.009
Piezoelectric layer thickness	0.0002 m		

voltage. Moreover, the closer the parasitic beam is to the fixed (clamping) end of the host beam, the lower the generated voltage is. The voltage generated by the piezoelectric element on the parasitic beam near the root of the host beam is quite small for practical use.

B. Modified piezoelectric metamaterial beam—Model A

In this section, a finite element model, termed Model A (Fig. 11), of the modified metamaterial beam, is developed to validate the theoretical studies presented in Sec. II. In Model A, one-dimensional 2-node spring elements (COMBIN14) were used to realize the alternate coupling of local resonators with a spring stiffness of 6912 N/m. It is worth noting that the coupling spring stiffness here is half of that in the analytical model ($k_c = 13\,824 \text{ N/m}$ in Sec. II C) because each oscillator in the analytical model is equivalent to a pair of cantilever beams. The two vertical DOFs of the spring were coupled with the vertical DOFs of the centres of the left- and right-hand-side parasitic beam tip masses, respectively. Other boundary conditions are the same as used in the conventional model.

1. Vibration suppression of Model A

Figure 12(a) shows the transmittance predicted by Model A. It can be observed that the first band gap (87.4–121.6 Hz) is almost the same as that of the conventional one. An additional band gap (152.6–158.3 Hz) appears to exist although it is relatively narrow compared with the first one. Figure 12(b) compares the results from FE Model A and the analytical predictions in Sec. II. It is noted that their predictions of band gaps are qualitatively in good agreement. However, though the parameters of the parasitic beam and the coupling spring are carefully selected to make Model A behave as closely as possible to the analytical model with the lumped resonator mass (Fig. 5), the results are not completely consistent. This is because the parasitic beams can cause torsional motion though this effect was minimized by symmetrically attaching parasitic beams onto the host beam.

To further explore the phenomenon of the second band gap in the internally coupled metamaterial beam, Fig. 13 shows the steady state vibration amplitude of the conventional metamaterial beam and the modified metamaterial beam (Model A) at 156.22 Hz (which is within the second

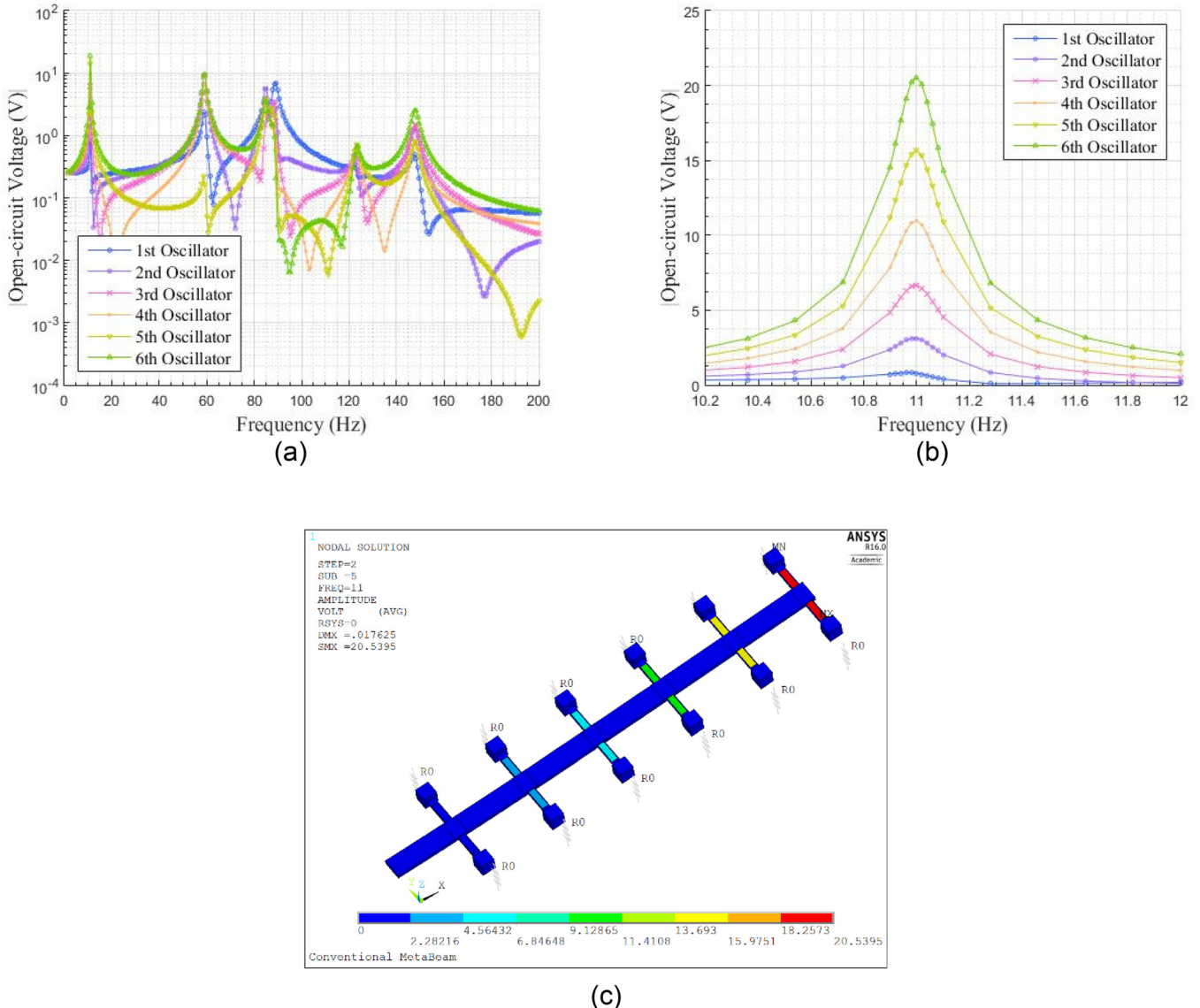


FIG. 10. Open circuit voltage responses of piezoelectric elements embedded in the conventional metamaterial beam: (a) over the spectrum of 0–200 Hz; (b) around the first resonance with a higher resolution; and (c) open circuit voltage contour at 11 Hz.

band gap of Model A). As compared to the conventional metamaterial beam, the vibration of Model A is suppressed significantly. The vibration energy of the host beam decays with an increase in the distance from the clamping end. It is worth noting that the resonant frequency of the parasitic beam is around 90 Hz, and the vibration suppression phenomenon at 156.22 Hz is due to the existence of the coupling spring.

2. Energy harvesting of Model A

The open circuit voltage responses over the whole frequency range of the piezoelectric elements bonded onto those 6 pairs of parasitic beams of Model A are demonstrated in Fig. 14(a). It is noted that around the first resonant frequency, these piezoelectric elements provide the largest open circuit voltages. Similarly, with a high frequency resolution, Fig. 14(b) shows the responses around the first peak with higher resolution. It can be found that the maximum voltage amplitude of 80.08 V is achieved at a frequency of

14.12 Hz which represents a 290% increase as compared to that of the conventional metamaterial beam PEH [Fig. 10(b)]. This indicates that the energy harvesting performance of Model A is much improved due to the existence of the internal coupling.

The steady state open circuit voltage contour at 14.12 Hz is demonstrated in Fig. 14(c). It is noted that the electrical potential distribution is different from that of the conventional metamaterial beam PEH. Due to the existence of the internal coupling, the piezoelectric element at the utmost tip no longer provides the largest voltage output. The 5th parasitic beam seems to be the most efficient one. Overall, all the piezoelectric elements' voltage outputs [Fig. 14(b)] have been significantly enhanced as compared to those of the conventional metamaterial beam PEH [Fig. 10(b)]. Therefore, from the perspective of energy harvesting, the introduction of the internal coupling is favourable. This is also consistent with what was concluded in the analytical study.

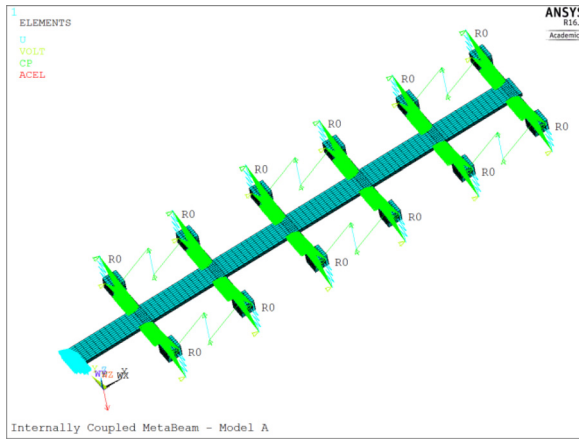
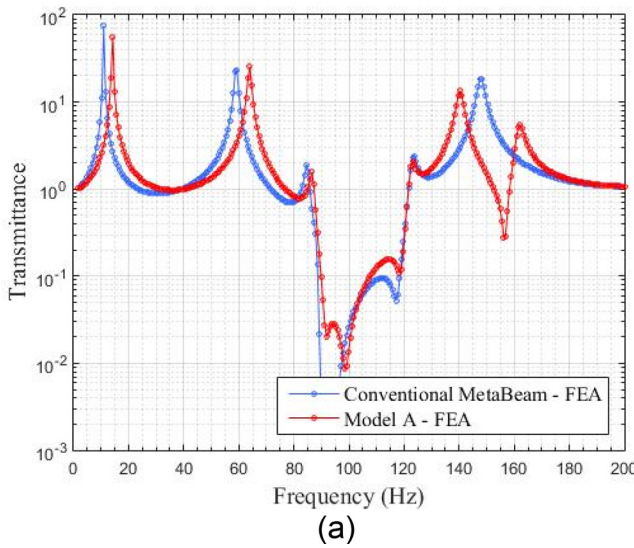
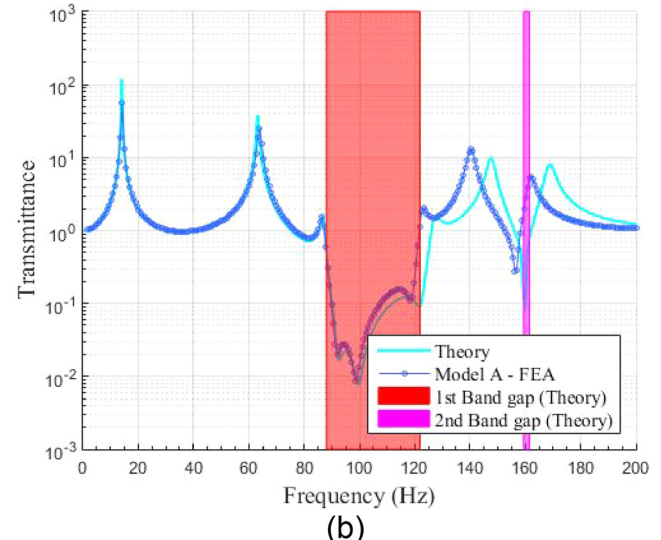


FIG. 11. Finite element model A of the internally coupled metamaterial beam embedded with piezoelectric elements.

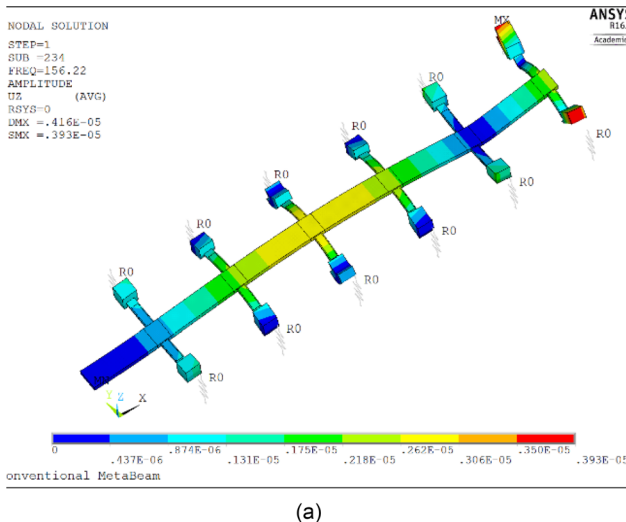


(a)

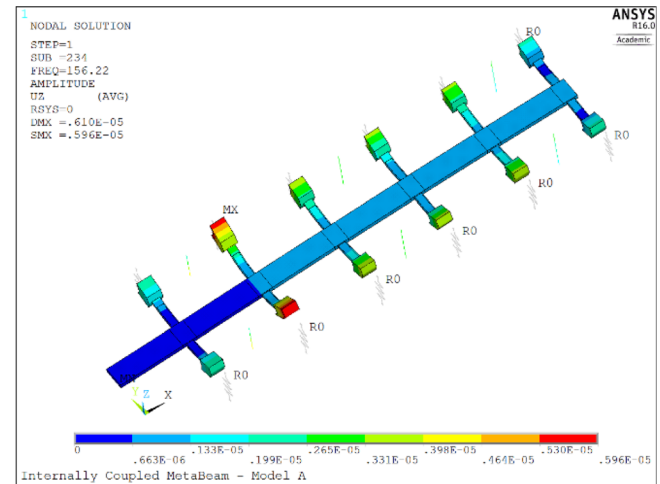


(b)

FIG. 12. (a) Comparison of transmittances of the internally coupled metamaterial beam (Model A) and the conventional metamaterial beam from finite element analysis and (b) comparison of FE Model A with the analytical results.



(a)



(b)

FIG. 13. Steady state vibration amplitude contours of (a) conventional metamaterial beam and (b) internally coupled metamaterial beam—Model A at 156.22 Hz.

C. Modified piezoelectric metamaterial beam—Model B

Considering that the internal coupling between local resonators of Model A is not easy to achieve in reality, an alternative finite element model B (Model B) that is more practical in respect of the implementation of the internal coupling is established (Fig. 15). In this model, the internal coupling spring is replaced by a thin beam, which connects the tip masses of the left- and right-hand-side parasitic beams. The material properties of the connection beam are the same as those of the host beam. The geometry parameters are as follows: width is 0.008 m, thickness is 0.001 m, and length which is equal to 0.0614 m is determined by other dimension parameters of the metamaterial beam. The connection beam is roughly considered as a guided beam.³⁴ Theoretically, the effective stiffness of such kind of beam is 6912 N/m. It can

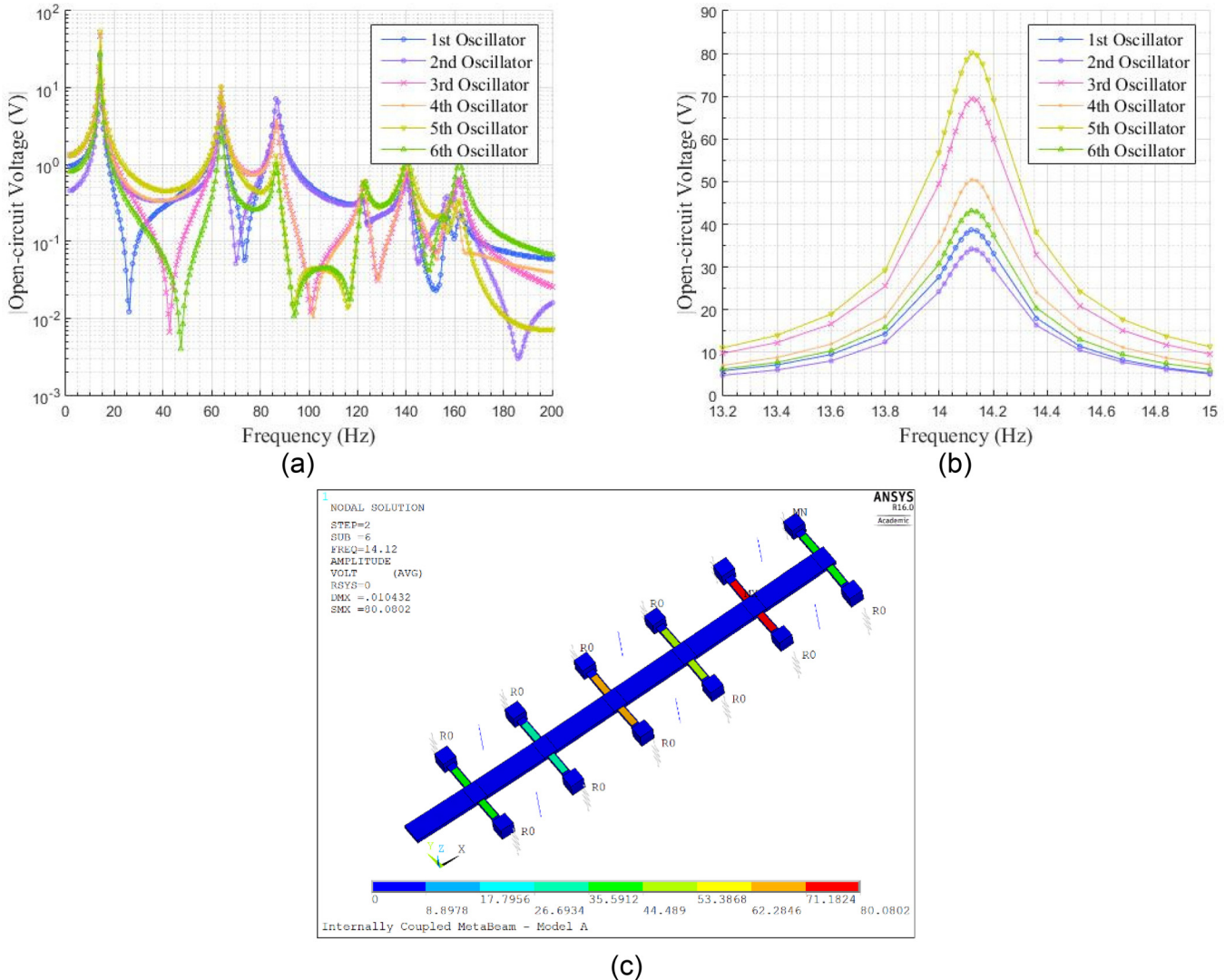


FIG. 14. Open circuit voltage responses of the piezoelectric elements embedded in the internally coupled metamaterial beam—Model A: (a) over spectrum of 0–200 Hz, (b) around first resonance with a higher resolution, and (c) open circuit voltage contour at 14.12 Hz.

be noted that these parameters are carefully selected to make the beam connection roughly comparable with the spring connection in Model A. The excitation and other boundary conditions remain the same as those in Model A.

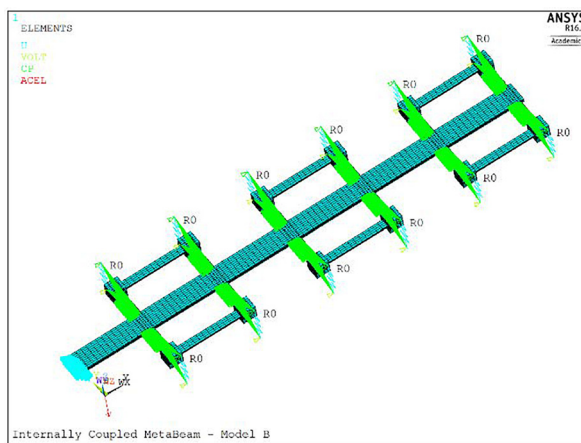


FIG. 15. Finite element model B of the internally coupled metamaterial beam embedded with piezoelectric elements.

1. Vibration suppression of Model B

Figure 16 shows the transmittance predicted by Model B. Like Model A, the width of the first band gap (83.3–115.8 Hz) has a minor difference as compared to the conventional metamaterial beam (85.9–121.7 H), but the band gap moves towards low frequency slightly. There also appears an additional second band gap (125.6–156.2 Hz). However, the behaviour of the second band gap is quite different from that of both Model A and the analytical study [Fig. 12(b)]. The width of the second band gap is much larger than the analytical prediction and becomes comparable to the width of the first band gap.

To further investigate the vibration behaviour of the system in the second band gap, Fig. 17 presents the steady state vibration amplitude contours of the conventional metamaterial beam (FE model), Model A and Model B at 142.29 Hz (within the 2nd band gap of Model B). It is to be noted that the vibration of Model B is significantly suppressed. The vibration energy decays rapidly along the length of the host beam.

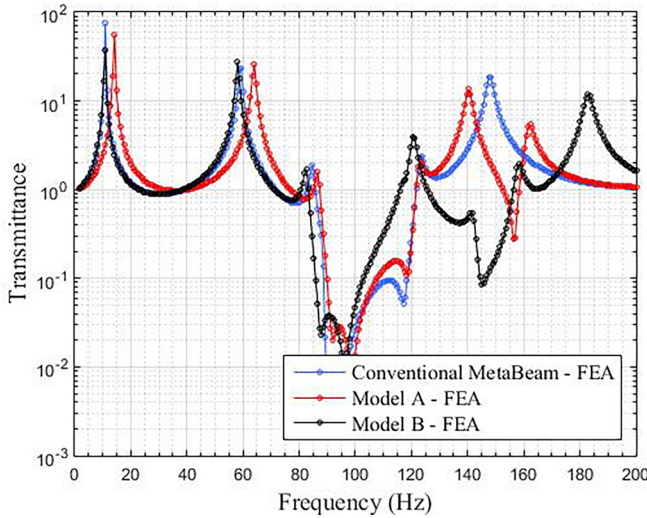


FIG. 16. Comparison of transmittances of the internally coupled metamaterial beam (Models A & B) and the conventional metamaterial beam from finite element analysis.

2. Energy harvesting of Model B

The open circuit voltage frequency responses of the piezoelectric elements bonded onto those 6 pairs of parasitic beams of Model B are shown in Fig. 18(a). Around the first

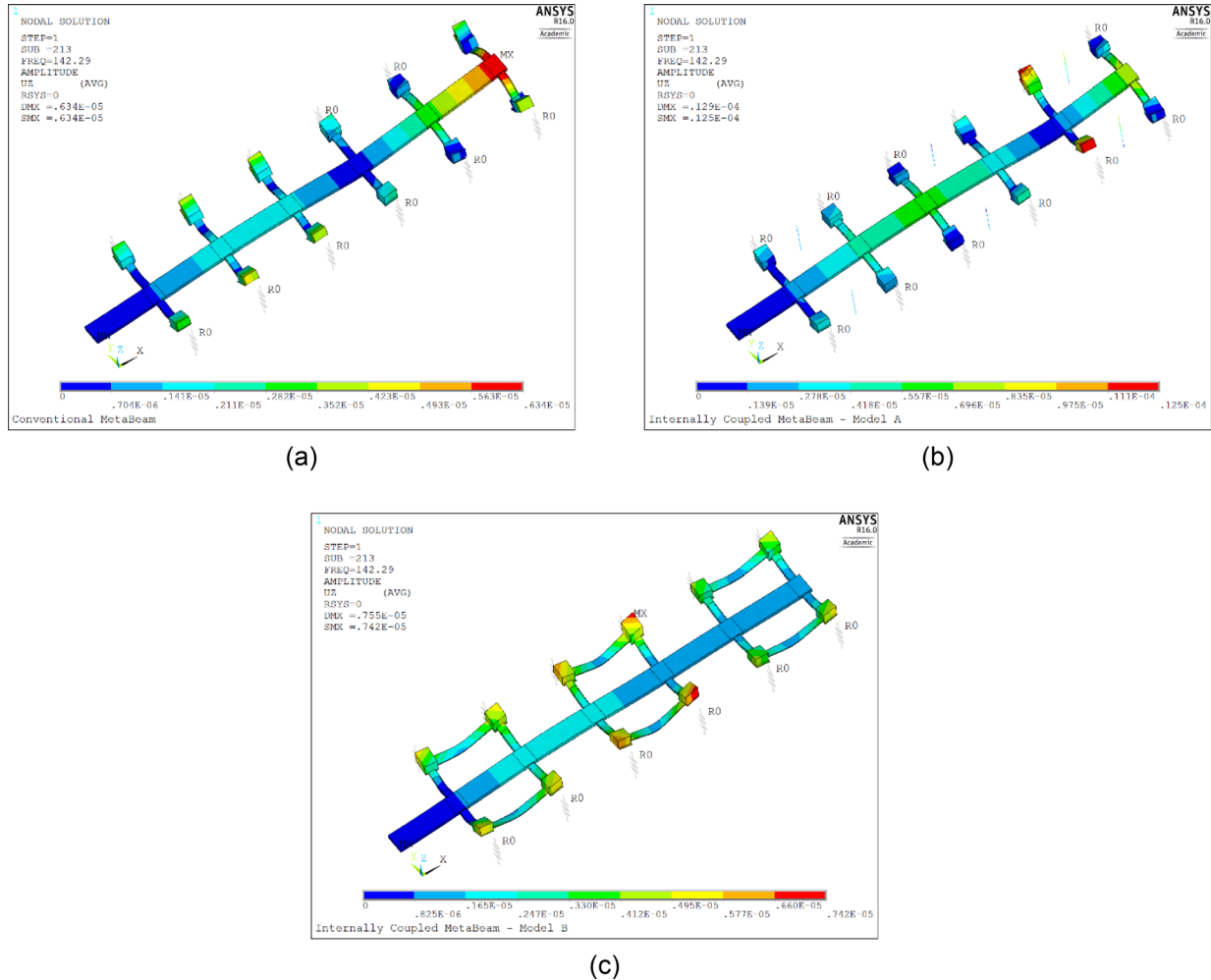


FIG. 17. Steady state vibration amplitude contours of (a) conventional metamaterial beam, (b) internally coupled metamaterial beam—Model A, and (c) internally coupled metamaterial beam—Model B at 142.29 Hz.

resonant frequency, these piezoelectric elements provide the largest open-circuit voltages, as expected. Figure 18(b) shows the responses around the first peak with a higher frequency resolution. The corresponding steady state open circuit voltage contour plot is shown in Fig. 18(c).

In contrast to Model A, the enhancement in the voltage output observed in Model B is not obvious, and the maximum voltage amplitude of Model B is even slightly decreased to 20.50 V as compared to that of the conventional one [Fig. 10(b)]. Although the voltage output of the 6th piezoelectric element remains almost unchanged, the voltage output of the 5th one is enhanced from 15.68 to 19.05 V, providing a similar energy harvesting ability as that of the 6th element [Fig. 18(b)]. This is because near the first resonant frequency, motions of all parasitic beams are almost in phase (but not completely because of damping). The introduction of connection beams forced the neighbouring two coupled parasitic beams to behave the same. Overall, the energy harvesting performance of Model B is improved as compared to that of the conventional metamaterial beam PEH.

IV. CONCLUSIONS

This paper has proposed and investigated an internally coupled metamaterial beam embedded with piezoelectric

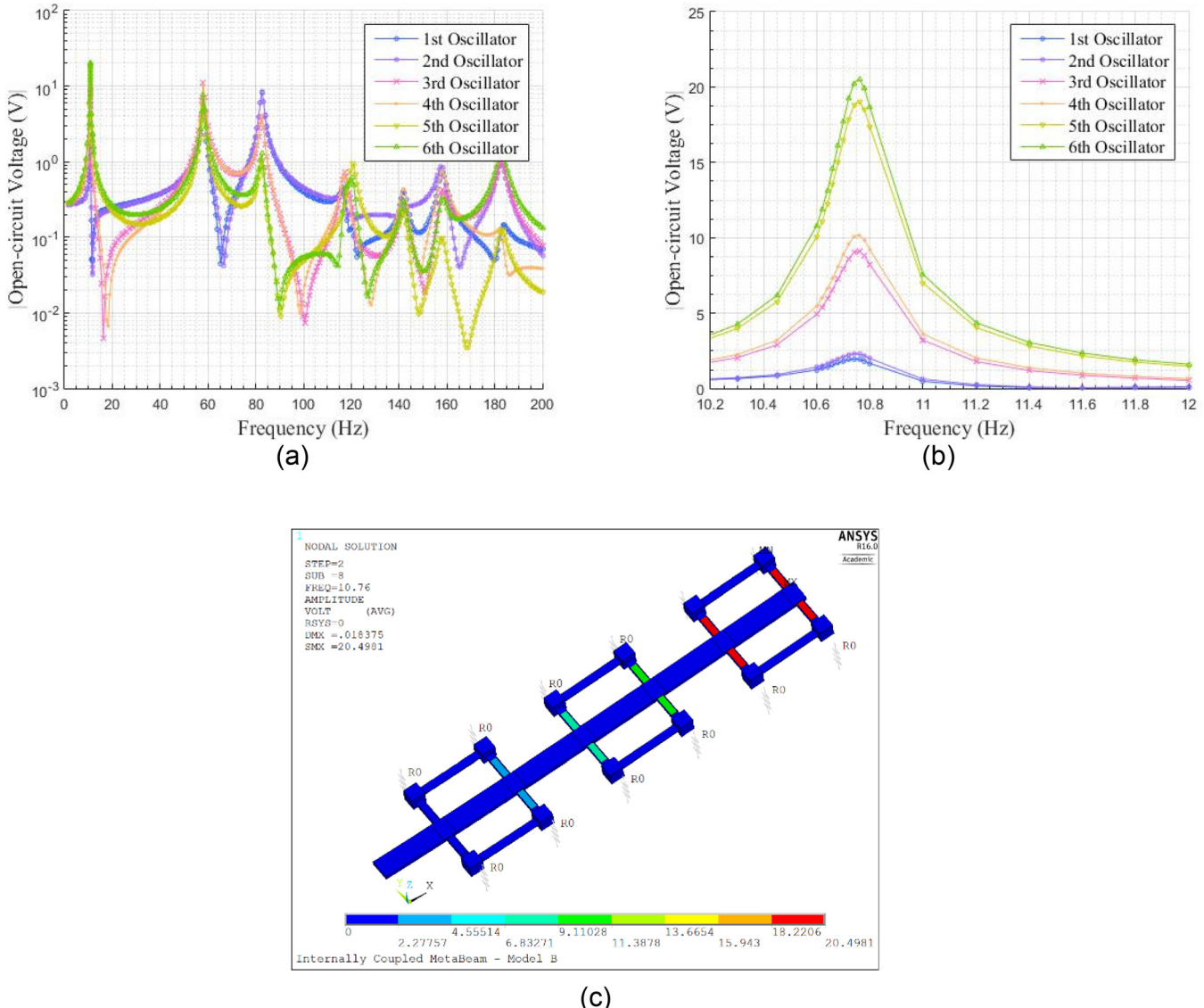


FIG. 18. Open circuit voltage responses of embedded piezoelectric elements in the internally coupled metamaterial beam—Model B: (a) over spectrum of 0–200 Hz, (b) around first resonance with a higher resolution, and (c) open circuit voltage contour at 10.76 Hz.

elements for simultaneous vibration suppression and energy harvesting. Both the band structure of an infinite long model and the transmittance of a finite long model have been analysed. This demonstrated the occurrence of an additional band gap due to the existence of the internal coupling. The theoretical study also shows that not only the vibration suppression ability can be slightly enhanced, but also the energy harvesting performance can be significantly improved by using the modified metamaterial beam, as compared to the conventional one without internal coupling.³¹ In addition to the analytical models, a finite element model (Model A), which is equivalent to the analytical model in respect of the internal coupling, is developed. The FE results are in good agreement with the analytical model and confirm both the vibration suppression and energy harvesting performance improvement of the proposed internally coupled metamaterial beam PEH. Another finite element model (Model B), which incorporates more practical implementation, is also established in

which the internal coupling is realized by a thin beam connection rather than an ideal spring connection. It is found that although the internal coupling using such a beam connection does not provide much improvement in energy harvesting as compared to the conventional metamaterial beam PEH, the vibration suppression ability is greatly improved with a much wider second band gap than that obtained from Model A. The analytical models and the finite element models developed in the work provide useful tools to design internally coupled piezoelectric metamaterial beams for concurrent efficient energy harvesting and vibration suppression.

ACKNOWLEDGMENTS

This work was financially supported by the Energy Education Trust of New Zealand (Grant No. 3708242) and the Ph.D. scholarship from the China Scholarship Council (Grant No. 201608250001).

- ¹V. M. Shalaev, W. Cai, U. K. Chettiar, H. K. Yuan, A. K. Sarychev, V. P. Drachev, and A. V. Kildishev, "Negative index of refraction in optical metamaterials," *Opt. Lett.* **30**(24), 3356–3358 (2005).
- ²J. Yao, Z. Liu, Y. Liu, Y. Wang, C. Sun, G. Bartal, A. M. Stacy, and X. Zhang, "Optical negative refraction in bulk metamaterials of nanowires," *Science* **321**(5891), 930 (2008).
- ³H. Huang and C. Sun, "Anomalous wave propagation in a one-dimensional acoustic metamaterial having simultaneously negative mass density and Young's modulus," *J. Acoust. Soc. Am.* **132**(4), 2887–2895 (2012).
- ⁴X. Liu, G. Hu, G. Huang, and C. Sun, "An elastic metamaterial with simultaneously negative mass density and bulk modulus," *Appl. Phys. Lett.* **98**(25), 251907 (2011).
- ⁵S. Yao, X. Zhou, and G. Hu, "Experimental study on negative effective mass in a 1D mass-spring system," *New J. Phys.* **10**(4), 043020 (2008).
- ⁶H. Huang, C. Sun, and G. Huang, "On the negative effective mass density in acoustic metamaterials," *Int. J. Eng. Sci.* **47**(4), 610–617 (2009).
- ⁷J. Xu and J. Tang, "Tunable prism based on piezoelectric metamaterial for acoustic beam steering," *Appl. Phys. Lett.* **110**(18), 181902 (2017).
- ⁸K. M. Ho, Z. Yang, X. Zhang, and P. Sheng, "Measurements of sound transmission through panels of locally resonant materials between impedance tubes," *Appl. Acoust.* **66**(7), 751–765 (2005).
- ⁹M. Oudich, M. B. Assouar, and Z. Hou, "Propagation of acoustic waves and waveguiding in a two-dimensional locally resonant phononic crystal plate," *Appl. Phys. Lett.* **97**(19), 193503 (2010).
- ¹⁰L. Shen, J. Wu, S. Zhang, Z. Liu, and J. Li, "Low-frequency vibration energy harvesting using a locally resonant phononic crystal plate with spiral beams," *Mod. Phys. Lett. B* **29**(1), 1450259 (2015).
- ¹¹X. Zhou and G. Hu, "Superlensing effect of an anisotropic metamaterial slab with near-zero dynamic mass," *Appl. Phys. Lett.* **98**(26), 263510 (2011).
- ¹²R. Zhu, X. Liu, G. Hu, C. Sun, and G. Huang, "A chiral elastic metamaterial beam for broadband vibration suppression," *J. Sound Vib.* **333**(10), 2759–2773 (2014).
- ¹³Y. Liu, D. Yu, L. Li, H. Zhao, J. Wen, and X. Wen, "Design guidelines for flexural wave attenuation of slender beams with local resonators," *Phys. Lett. A* **362**(5), 344–347 (2007).
- ¹⁴Y. Xiao, J. Wen, L. Huang, and X. Wen, "Analysis and experimental realization of locally resonant phononic plates carrying a periodic array of beam-like resonators," *J. Phys. D: Appl. Phys.* **47**(4), 045307 (2013).
- ¹⁵N. Gao, J. Wu, H. Hou, and L. Yu, "Excellent low-frequency sound absorption of radial membrane acoustic metamaterial," *Int. J. Mod. Phys. B* **31**(3), 1750011 (2017).
- ¹⁶G. W. Milton and J. R. Willis, "On modifications of Newton's second law and linear continuum elastodynamics," *Proc. R. Soc. London, Ser. A* **463**, 855–880 (2007).
- ¹⁷H. Huang and C. Sun, "Wave attenuation mechanism in an acoustic metamaterial with negative effective mass density," *New J. Phys.* **11**(1), 013003 (2009).
- ¹⁸D. Yu, Y. Liu, G. Wang, H. Zhao, and J. Qiu, "Flexural vibration band gaps in Timoshenko beams with locally resonant structures," *J. Appl. Phys.* **100**(12), 124901 (2006).
- ¹⁹P. F. Pai, "Metamaterial-based broadband elastic wave absorber," *J. Intell. Mater. Syst. Struct.* **21**(5), 517–528 (2010).
- ²⁰C. Sugino, Y. Xia, S. Leadenham, M. Ruzzene, and A. Erturk, "A general theory for bandgap estimation in locally resonant metastructures," *J. Sound Vib.* **406**, 104–123 (2017).
- ²¹A. Banerjee, R. Das, and E. P. Calfus, "Frequency graded 1D metamaterials: A study on the attenuation bands," *J. Appl. Phys.* **122**(7), 075101 (2017).
- ²²G. Huang and C. Sun, "Band gaps in a multiresonator acoustic metamaterial," *J. Vib. Acoust.-Trans. ASME* **132**(3), 031003 (2010).
- ²³Y. Chen, G. Huang, and C. Sun, "Band gap control in an active elastic metamaterial with negative capacitance piezoelectric shunting," *J. Vib. Acoust.* **136**(6), 061008 (2014).
- ²⁴G. Hu, L. Tang, A. Banerjee, and R. Das, "Metastructure with piezoelectric element for simultaneous vibration suppression and energy harvesting," *J. Vib. Acoust.* **139**(1), 011012 (2017).
- ²⁵G. Hu, L. Tang, R. Das, S. Gao, and H. Liu, "Acoustic metamaterials with coupled local resonators for broadband vibration suppression," *AIP Adv.* **7**(2), 025211 (2017).
- ²⁶Y. Zhou, P. Wei, Y. Li, and Q. Tang, "Continuum model of acoustic metamaterials with diatomic crystal lattice," *Mech. Adv. Mater. Struct.* **24**(13), 1059–1073 (2017).
- ²⁷A. Erturk and D. J. Inman, "A distributed parameter electromechanical model for cantilevered piezoelectric energy harvesters," *J. Vib. Acoust.* **130**(4), 041002 (2008).
- ²⁸L. Tang, Y. Yang, and C. K. Soh, "Toward broadband vibration-based energy harvesting," *J. Intell. Mater. Syst. Struct.* **21**(18), 1867 (2010).
- ²⁹J. Xu and J. Tang, "Modeling and analysis of piezoelectric cantilever-pendulum system for multi-directional energy harvesting," *J. Intell. Mater. Syst. Struct.* **28**(3), 323–338 (2017).
- ³⁰K. Mikoshiba, J. M. Manimala, and C. Sun, "Energy harvesting using an array of multifunctional resonators," *J. Intell. Mater. Syst. Struct.* **24**(2), 168–179 (2013).
- ³¹G. Hu, L. Tang, and R. Das, "Metamaterial-inspired piezoelectric system with dual functionalities: energy harvesting and vibration suppression," *Proc. SPIE* **101641**, 101641X (2017).
- ³²Z. Chen, B. Guo, Y. Yang, and C. Cheng, "Metamaterials-based enhanced energy harvesting: A review," *Physica B* **438**, 1–8 (2014).
- ³³O. Aldraihem and A. Baz, "Energy harvester with a dynamic magnifier," *J. Intell. Mater. Syst. Struct.* **22**(6), 521–530 (2011).
- ³⁴J. M. Gere and B. J. Goodno, *Mechanics of Materials* (Cengage Learning, 2011).